Numerical Heat Transfer, Part A: Applications: An International Journal of Computation and Methodology
Publication details, including instructions for authors and subscription information:
http://www.tandfonline.com/loi/unht20

Modeling of Valveless Micropumps

Yeng-Yung Tsui [a] & Shin-En Wu [a]
[a] Department of Mechanical Engineering , National Chiao Tung University , Taiwan, Republic of China
Published online: 10 Dec 2009.

To cite this article: Yeng-Yung Tsui & Shin-En Wu (2009) Modeling of Valveless Micropumps, Numerical Heat Transfer, Part A: Applications: An International Journal of Computation and Methodology, 56:9, 727-745, DOI: 10.1080/10407780903466089

To link to this article: http://dx.doi.org/10.1080/10407780903466089

Numerical Heat Transfer, Part A, 56: 727–745, 2009

ISSN: 1040-7782 print/1521-0634 online
DOI: 10.1080/10407780903466089

Taylor & Francis
Taylor & Francis Group

MODELING OF VALVELESS MICROPUMPS

Yeng-Yung Tsui and Shin-En Wu
Department of Mechanical Engineering, National Chiao Tung University, Taiwan, Republic of China

There are two difficulties encountered in modeling valveless micropumps using lumped-element methods. The pressure loss coefficient for fluidic diodes used in valveless pumps to rectify flow depends on the flow direction. A problem arises in choosing the proper loss correlation because the flow direction is not known a priori. Another problem is the quadratic form of the equation for the flow through the fluidic diodes, which brings about multiple solutions. The above problems become even more serious in multi-chamber cases. They are overcome in this study by suitably formulating the flow resistance. In addition, the flow inertia is accounted for in the unsteady model. The steady and unsteady models are evaluated by comparing with CFD simulations, which also serve to illustrate the flow field in more detail. It is shown that, compared with the steady model, the variation of the flow rate and pressure predicted by the unsteady model behaves in a close manner to those obtained by multidimensional calculations.

INTRODUCTION

The piston-like reciprocating pumps rely on oscillations [1–3] of mechanical parts to displace fluids. Flexible diaphragms activated by piezoelectric, thermopneumatic, and electrostatic actuators, among others, are usually used to fulfill the reciprocation function. It is common for these pumps to incorporate check valves to rectify the flow. During the supply mode of the pumping procedure, the check valve at inlet is opened to allow fluid to enter the pump chamber as a result of the underpressure created by the retreat of the diaphragm. The fluid is then repelled out of the chamber through the outlet valve in the pump mode by reversing the motion of the diaphragm. In microsystems, the sizes of the consisted devices are in the scales ranging from several microns to millimeters. As a consequence of miniaturization, micropumps in particle-delivering systems have to take a risk of blocking by the particles present in the passage of the check valve. Besides, it is easy to cause wear and fatigue of the mechanical valves during the oscillating movement of these valves. Further, the manufacture of this kind of valves is difficult.

To avoid the problems above, the valveless micropump concept was introduced. In these micropumps, the valves are replaced by fluidic diodes which do

Received 17 April 2009; accepted 14 October 2009.
The support of the National Science Council of the Republic of China is acknowledged.
Address correspondence to Yeng-Yung Tsui, Department of Mechanical Engineering, National Chiao Tung University, 1001 Ta-Hsueh Road, Hsinchu 300, Taiwan, Republic of China. E-mail: yytsui@mail.nctu.edu.tw

NOMENCLATURE

A_t, A_l	areas at the two sides of the nozzle/diffuser element	R	flow resistance of the nozzle/diffuser element
h_m	maximum deflection amplitude	t	time
K_d, K_n	loss coefficients of the diffuser and the nozzle	T	one oscillating period
l	the length of the nozzle/diffuser element	V_m	maximum deflection amplitude of the volume swept by the membrane
L	flow inductance of the nozzle/diffuser element	U	mean velocity
P	pressure	$\vec{V}$	velocity vector
P_b	back pressure at the outlet	w	time-dependent variation of the deflection of the membrane
P_{in}, P_{out}	pressures at the inlet and outlet	β	ratio of Q_{out} to Q_{in}
P_t, P_l	pressures at the two sides of the nozzle/diffuser element	η_R	real efficiency
P_1, P_2	pressures in the chambers 1 and 2 of the micropump	η_1, η_2	approximate efficiencies
Q	volumetric flow rate	μ	fluid viscosity
Q_{in}, Q_c, Q_{out}	flow rates through the inlet, central, and outlet nozzle/diffusers	ρ	fluid density
r	radial distance	ω	angular frequency of oscillation
r_t, r_0	radius of the piezo disc and the pump chamber	**Subscripts**	
		p	pumping stage
		s	supply stage
		Superscripts	
		o	old values

not have any moving parts. The resistance of the fluid flow through these devices depends on the flow direction. For a specified pressure difference across the fluidic diode, the flow rate is higher in the forward direction than in the reverse direction. This results in a net flow in the preferential direction.

Vortex diodes are a kind of fluidic diode that can be found in various engineering applications to regulate flow in macro scales. Works have been made to investigate the influence of various parameters and to optimize the design of such devices [4–6]. Realization of this concept in microfluidic flows was carried out recently by Anduze et al. [7]. Another type of fluidic diode is the valvular conduit of Tesla [8], which was first applied to microsystems by Forster et al. [9]. Its characteristics in microflows were examined by Turowski et al. [10]. The geometry of this valve was optimized by Gamboa et al. [11]. The simplest device to suit the purpose of rectification of fluid flow is the nozzle/diffuser. It was incorporated in micropumps by Stemme and Stemme [12] and Gerlach and Wurmus [13]. The flow characteristics of this device in either flat-wall type or circular type were investigated by Olsson et al. [14, 15] and Singhal et al. [16].

The development of CFD technologies has made them an important tool to help engineers to tackle flow problems of increasing complexity. However, it is costly to solve the Navier-Stokes equations, especially for three-dimensional, unsteady flows. In the preliminary stage of design or optimization of a large system, it is common to model the system with a simple approach. The different parts of the system are modeled as lumped elements with appropriate approximation of equations.

These elements are then linked together to form a network which is ready for rapid analysis [17, 18].

The valveless micropump incorporating nozzle/diffusers to rectify the pumping flow is the main concern of this study. This kind of micropump has bean analyzed using lumped-system methods by several researchers [19–25]. The basic concept for the lumped system is the conservation of overall mass fluxes into and out of the pump chamber. Ullman [19] introduced a blocking pressure to account for the stiffness of the piezoelectric membrane, which leads to a differential equation for the mass conservation over the chamber. The model of Olsson et al. [20] is based on conservation of both mass and energy. The interaction between the membrane and the fluid flow is taken into account by including the piezoelectric force and the chamber pressure in the momentum balance over the membrane. In the studies of Pan et al. [21, 22], the vibration of the membrane was simulated using an unsteady partial differential equation, based on the bending theory of thin plate. In the models of Ullmann and coworkers [23, 24], the deformation of the membrane is assumed to be a clamped or supported disk under the action of a concentrated force acting on the center. The inertias of the membrane as well as the entire fluid in the system are included in the dynamic simulation. In a recent study of Tsui and Lu [25], the flow in a valveless pump was analyzed using a static lumped-system analysis and the CFD simulation. It was shown that the resulting inlet- and outlet-flow variations and the pumping efficiencies obtained from the lump model are close to the predictions by the CFD method and experimental data for various back pressures.

In modeling of valveless micropump, it is essential to relate the pressure difference ΔP across the nozzle/diffuser element and the velocity through it. This relation is usually given in the form

$$\Delta P = \frac{K}{2}\rho U^2 \tag{1}$$

where K is the loss coefficient and U the mean velocity at the throat of the nozzle/diffuser. The loss coefficient K is a function of the velocity as well as the flow direction. This element functions as a diffuser in one flow direction and becomes a nozzle in the other direction. This causes difficulties in solving the system of equations of the flow problems because, in general, the flow direction is not known a priori. To overcome this problem, the pumping process was divided into several modes in which the flow direction is determined according to the sign of the pressure difference across this element [19, 21, 23, 25]. This situation becomes even worse when multiple chambers are included in the micropump. Another difficulty encountered is that the quadratic form in terms of velocity leads to non-unique solutions. It will be shown in the following that the relation can be arranged in a form by which an unique solution can be obtained without the need to divide the pumping process into different modes for a micropump system with multi-chamber. In addition to the lumped-system analysis, multidimensional calculations are also conducted in the present study to illustrate the complicated flow structure in the pump system and to validate the developed models.

LUMP MODEL

The micropump considered in this study includes one or two chambers, along with several nozzle/diffusers to connect the chambers and the inlet and outlet. The resistance to the flow through the nozzle/diffusers is the main concern in the modeling. The chamber has a relatively large volume. Compared with the chamber, the displacement of the oscillating membrane is assumed to be insignificant. Therefore, the flow resistance in the chamber is ignored for this low-compression ratio pump in our model.

The relation of Eq. (1) between the pressure difference and the velocity can be rewritten as

$$P_t - P_l = K_d \frac{\rho}{2A_t^2} Q^2, \quad P_t > P_l \tag{2a}$$

$$P_l - P_t = K_n \frac{\rho}{2A_t^2} Q^2, \quad P_t < P_l \tag{2b}$$

where, as seen in Figure 1, P_t and P_l are the pressures at the throat on the left side and that on the right side of the element, Q is the volumetric flow rate through it, A_t the area of the throat, and K_d and K_n are the loss coefficients corresponding to the functions of diffuser and nozzle, respectively. The flow rate is assumed to be positive in the direction from the left to the right, or from the inlet to the outlet in the pumping system. The above two relations can be combined into a single form.

$$P_t - P_l = \left[\max\left(\frac{Q}{|Q|}, 0\right) K_d - \min\left(\frac{Q}{|Q|}, 0\right) K_n\right] \frac{\rho}{2A_t^2} |Q| Q \tag{3}$$

This model does not include the flow unsteadiness. To account for the unsteady effects, an inertial term is added.

$$P_t - P_l = \left[\max\left(\frac{Q}{|Q|}, 0\right) K_d - \min\left(\frac{Q}{|Q|}, 0\right) K_n\right] \frac{\rho}{2A_t^2} |Q| Q + \frac{\rho l}{\frac{1}{2}(A_t + A_l)} \frac{dQ}{dt} \tag{4}$$

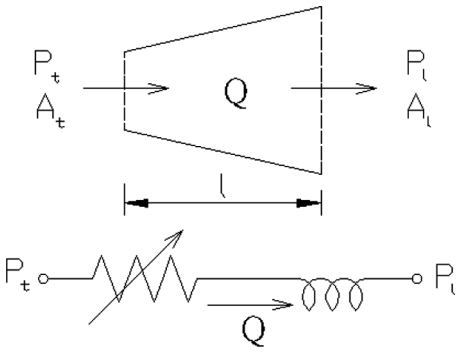

Figure 1. The nozzle/diffuser element and equivalent electrical circuit.

In the last term, l is the length of the nozzle/diffuser element and A_l is the cross-sectional area at the side opposite to the throat (see Figure 1).

The fluidic system can be represented by an electrical equivalent circuit with the flow rate analogous to the electrical current and the pressure to the voltage [17, 18]. The above equation can be interpreted as an R-L circuit (see Figure 1).

$$\Delta P = RQ + L\frac{dQ}{dt} \tag{5}$$

where R designates the flow resistance and L the inductance.

$$R = \left[\max\left(\frac{Q}{|Q|}, 0\right)K_d - \min\left(\frac{Q}{|Q|}, 0\right)K_n\right]\frac{\rho}{2A_l^2}|Q| \tag{6a}$$

$$L = \frac{\rho l}{\frac{1}{2}(A_t + A_l)} \tag{6b}$$

The resistance is variable, depending on the flow rate and the flow direction, and the inductance is constant for a specific nozzle/diffuser.

A micropump with two chambers under investigation is schematically sketched in Figure 2. The equations for the three nozzle/diffuser elements are expressed as

$$P_{\text{in}} - P_1 = R_{\text{in}}Q_{\text{in}} + \alpha L\frac{dQ_{\text{in}}}{dt} \tag{7a}$$

$$P_1 - P_2 = R_c Q_c + \alpha L\frac{dQ_c}{dt} \tag{7b}$$

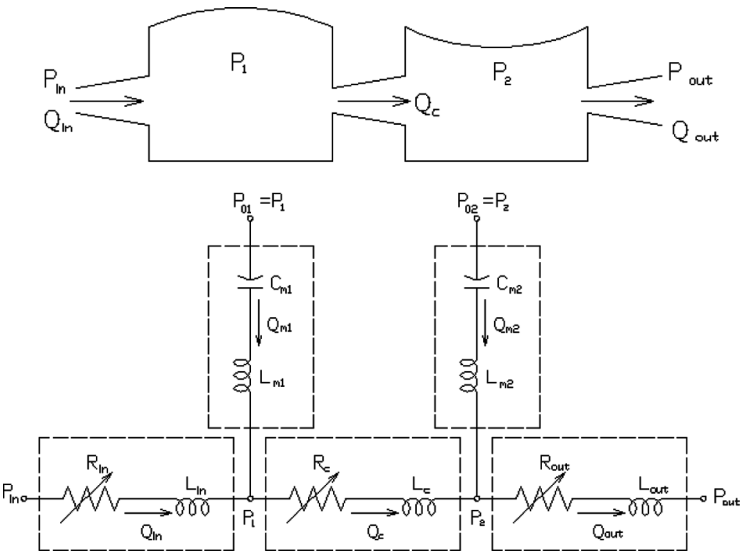

Figure 2. The valveless micropump with double chambers and equivalent electrical network.

$$P_2 - P_{\text{out}} = R_{\text{out}} Q_{\text{out}} + \alpha L \frac{dQ_{\text{out}}}{dt} \tag{7c}$$

where P_{in}, P_1, P_2, and P_{out} denote the pressures at the inlet, chamber 1, chamber 2 and the outlet, respectively, and Q_{in}, Q_c, and Q_{out} the flow rates through the inlet, central, and outlet nozzle/diffusers. The constant α is 1 for the unsteady model and 0 for the steady-state model. The inductances for the three nozzle/diffusers are the same because of identical elements used.

The membranes of the chambers are assumed to move in a harmonic motion, which is true if the driving frequency is much lower than the natural frequency of the membranes. Therefore, the conservation of mass for the two chambers gives

$$Q_c - Q_{\text{in}} = Q_{m1} = V_m \omega \sin(\omega t) \tag{8a}$$

$$Q_{\text{out}} - Q_c = Q_{m2} = V_m \omega \sin(\omega t + \delta) \tag{8b}$$

where V_m is the volume change amplitude of the vibrating membranes, ω the angular frequency of the vibration, and δ represents the difference in phase angle between the two membranes. The harmonic motion can be regarded as the homogeneous solution of an *L-C* circuit:

$$L_m \frac{dQ_m}{dt} + \frac{1}{C_m} \int Q_m dt = 0 \tag{9}$$

with $L_m C_m = 1/\omega^2$ and $L_m = \rho_m t_m / A_m$ (t_m is the thickness of the membrane and A_m the area), which is subject to the initial conditions.

$$Q_m(0) = V_m \omega \sin(\delta) \tag{10a}$$

$$Q'_m(0) = V_m \omega^2 \cos(\delta) \tag{10b}$$

The equivalent electrical network for the lumped system is displayed in Figure 2. It is noted that the force imposed on the membranes by the dynamic pressure in the chambers is ignored in this simulation ($P_{01} = P_1$ and $P_{02} = P_2$ in the network). For more accurate modeling, this effect can be included by imposing forcing terms $P_1 - P_{01}$ and $P_2 - P_{02}$ on the left-hand side of Eq. (9) for the two membranes.

To close the problem, the loss coefficients K_n and K_d need to be determined from either experiments or multidimensional calculations. The following correlations are adopted from reference [25] because the same nozzle/diffuser is used.

$$K_d = 1.315 \times 10^{-7} Q^{-0.921} + 0.5981 \tag{11a}$$

$$K_n = 1.173 \times 10^{-6} Q^{-0.8112} + 1.204 \tag{11b}$$

The differential equations can be discretized using the Euler implicit scheme or any other higher-order schemes. As an example, a finite difference analogue of Eq. (5)

is given as

$$L\frac{Q-Q^o}{\Delta t}+R^oQ=\Delta P \tag{12}$$

where the superscripts o denote the last time values and the flow resistance R^o is estimated using the old flow rate Q^o. The system of nonlinear algebraic equations arising from Eqs. (7) and (8) can easily be solved for Q_{in}, Q_c, Q_{out}, P_1, and P_2 using MATLAB.

MULTIDIMENSIONAL METHOD

The geometrical configuration of the two-chamber system is illustrated in Figure 3. The membranes of the pump, driven by piezoelectric disks, oscillate in a harmonic motion. The deflection of the membranes is assumed to distribute in a trapezoidal profile.

$$w(r,t)=-h_m\cdot\text{Min}\left(1,\frac{r_0-r}{r_0-r_1}\right)\cos(\omega t) \tag{13}$$

where r_0 is the radius of the chamber, r_1 that of the piezo disc, and h_m the maximum deflection at the center of the membrane. The maximum deflection is 1 μm, whereas the height of the chamber is 0.2 mm. Obviously, the change of the chamber volume caused by the membrane vibration is insignificant. To simplify the simulation, the volume of the chamber is assumed to be constant, i.e., the computational grid is fixed without motion. It is the oscillating velocity, obtained by differentiating the above equation, imposed on the membranes as boundary condition.

The flow is assumed to be incompressible. Due to the micro size of the pump, the Reynolds number is small, resulting in laminar flows. The conservation equations of mass and momentum are given by

$$\nabla\cdot\rho\vec{V}=0 \tag{14}$$

$$\frac{\partial\rho\vec{V}}{\partial t}+\nabla\cdot(\rho\vec{V}\otimes\vec{V})=-\nabla P+\mu\nabla^2\vec{V} \tag{15}$$

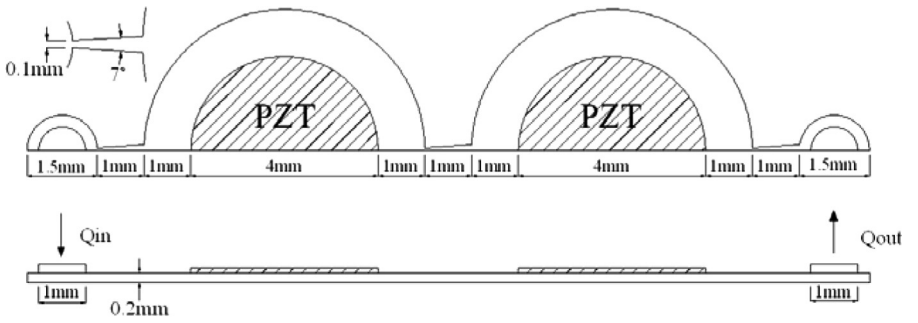

Figure 3. Configuration of the micropump with double chambers.

The differential equations are discretized using unstructured-grid techniques. Details of this method were described in references [26, 27]. A brief description is addressed in the following.

The equations are integrated over a control volume first. With the use of divergence theorem, the volume integrals of the convection and diffusion terms are transformed into surface integrals. The convective flux through the surface of the control volume is further approximated using a scheme blending the central difference and the upwind difference with a weighting biased toward the central difference. To handle the diffusive flux for the grid of arbitrary topology, an over-relaxed approach is employed.

All variables are collocated at the center of each cell. To avoid checkerboard oscillations arising in the non-staggered grid arrangement, the momentum interpolation method is used to obtain the velocities and, thus, the mass flux on the surface of the control volume. Similar to the SIMPLE algorithm, a pressure-correction equation is derived by forcing the mass fluxes through all the faces of the control volume to satisfy the continuity constraint. However, the SIMPLE algorithm relies on iteration around the momentum equation and the pressure-correction equation to tackle the coupling between them. This procedure is time-consuming for unsteady calculations. Therefore, the non-iterative, predictor-corrector procedure of PISO [28] is employed in this study. In the predictor step of this algorithm, the momentum equation is solved for the velocities using the prevailing pressure field. In the following corrector steps, the velocities and pressure are corrected via solving the pressure-correction equation obtained from mass conservation. In general, two corrector steps are sufficient to get rid of the mass residual left by the velocities in the predictor step.

As for boundary conditions, the no-slip condition is imposed on all solid walls except for the membranes where, as described above, oscillating velocities are prescribed. Pressures are specified at the openings of the inlet and outlet. In order to derive the flows through the open boundaries from the given pressures, a method, which ensures mass conservation at the mesh cells next to the boundaries, was adopted [25].

RESULTS AND DISCUSSION

Micropumps with single chamber and double chambers are under consideration. Zero pressure is assumed at the inlet and various back pressures are specified at the outlet. The membranes oscillate at a frequency of 2200 Hz. Only half the pump is considered in multidimensional calculations because of its geometric symmetry. Validation of the multidimensional method has been done in the study [25], in which a micropump with single chamber was considered. It was shown that with a suitable assumption of membrane deflection, good agreement with experimental measurements of net flow rate at various back pressures is obtained.

Single Chamber Case

The net flow rates for a number of back pressures predicted by both the steady and unsteady lump models and the multidimensional calculations are

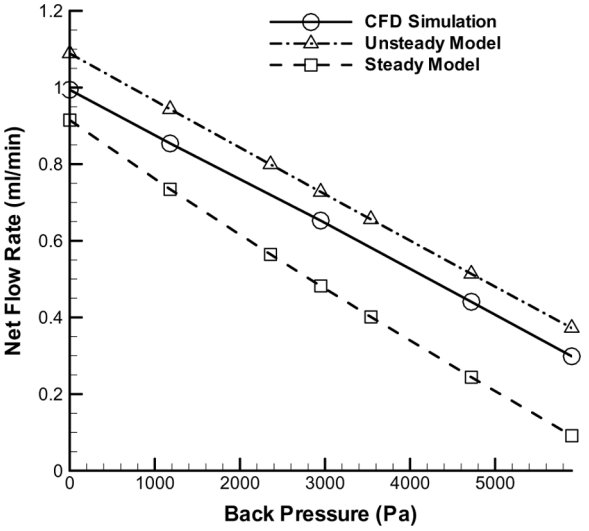

Figure 4. Comparison of predicted net flow rates for the single chamber case at various back pressures.

shown in Figure 4. A similar trend between the lumped-system analyses and the CFD calculations is observed, with higher flow rates for the lump models. The unsteady model gives better agreement than the steady model, which is further evidenced in Figure 5*a*, showing the time variation of both the inlet and outlet flow rates in one period for back pressure $P_b = 5900\,\text{Pa}$. It can be detected that the curves for the steady model is not as smooth as the others during the times at the beginning, end, and one half of a period. These times correspond to the transition stages between the pump and the supply modes. The non-smoothness is ascribed to the inertial effect not taken into account, which becomes significant when the driving velocity of the membrane is small in the transition stages [25]. In the steady model, the variation of flow rate is a direct reflection of the variation of the pressure in the chamber. As shown in Figure 5*b*, the chamber pressure varies in a sinusoidal-like manner for the steady model, which is of the same phase as the flow rates through the nozzle/diffuser elements shown in Figure 5*a*. Those for the unsteady model and the CFD simulation are similar to each other, but at a phase angle of about 90° different from that of the steady model. This phenomenon becomes clear through the following understanding. For constant flow resistance, the theoretical solution of Eq. (5) reveals that there is a phase difference angle $\tan^{-1}\omega L/R$ between the pressure difference ΔP and the flow rate Q. In our calculations, the ratio $\omega L/R$ falls in the range between 1 and 15, corresponding to phase angles 45° and 86°, respectively. The value 1 occurs at around $t = T/4$ and $3T/4$ and the value 15 at $t = 0$ and $T/2$. This means that at the start and middle of a period, the flow inertia dominates, resulting in about 90° phase angle; whereas, in the mid-half period, the effect of the flow resistance also plays an important role because the flow velocity is high at this stage. The instantaneous pressure at the center of the chamber close to the wall, obtained by

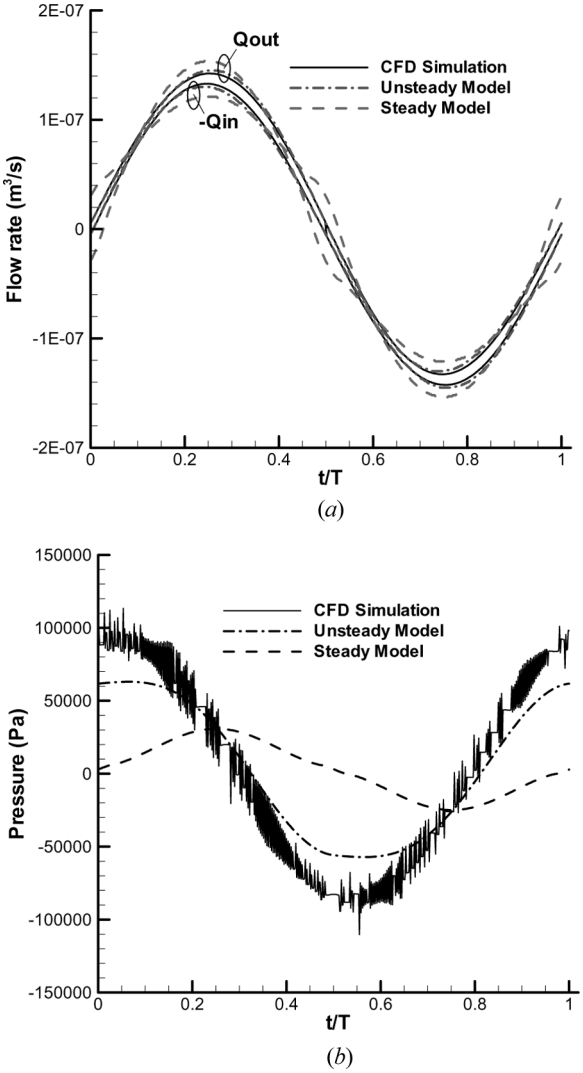

Figure 5. Variation of (*a*) the flow rates at the inlet and outlet and (*b*) the pressure in the chamber for the single chamber case at $P_b = 5900$ Pa.

the 3-D calculation, varies significantly with time due to the extremely complicated, unsteady flow formed in the chamber.

The real efficiency η_R of the pump is defined as the ratio of the net pumping flow volume to the volume swept by the reciprocating membrane in one period. An approximation to the efficiency can be expressed as [25]

$$\eta_1 = \frac{\omega}{2} \int_0^T (\beta(t) - 1) \sin(\omega t) dt \tag{16}$$

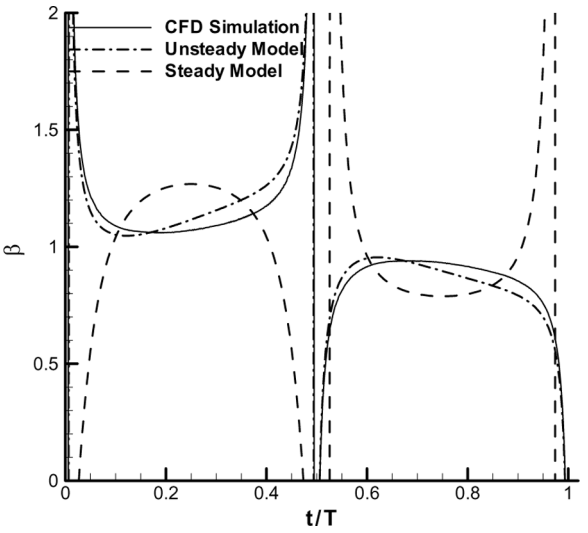

Figure 6. Comparison of flow rate ratios β obtained by the 3-D simulation and the two lump models for $P_b = 5900$ Pa.

where β is the ratio of the outlet flux to the inlet flux.

$$\beta(t) = \frac{Q_{\text{out}}}{Q_{\text{in}}} \tag{17}$$

As seen in Figure 6, the variation of the flux ratio of the unsteady lump model is similar to that of the multidimensional calculations, but not the steady model, especially at the transition times between the supply stages and the pump stages. A difficulty in utilizing Eq. (16) to estimate the pumping efficiency comes from the fact that the values of Q_{out} and Q_{in} approach zero during the transitions times, which results in a large variation of their ratio. To soothe the above problem, two mean flow ratios corresponding to the pump and supply stages are defined as

$$\beta_p = \frac{2}{T - 4a} \int_a^{T/2-a} \beta(t)dt \tag{18a}$$

$$\beta_s = \frac{2}{T - 4a} \int_{T/2+a}^{T-a} \beta(t)dt \tag{18b}$$

where the interval a is chosen as $T/20$ [25]. The mean flow ratios for different back pressures are shown in Figure 7. Substituting into Eq. (16) yields a simple form of pumping efficiency.

$$\eta_2 = \frac{1}{4}(\beta_p - \beta_s) \tag{19}$$

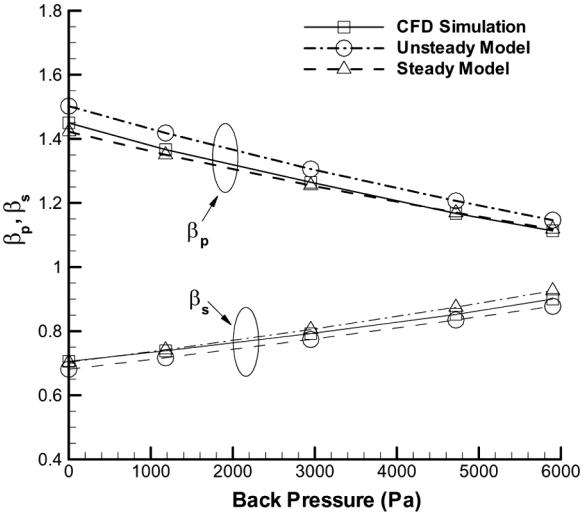

Figure 7. Comparison of mean flow rate ratios β_p and β_s obtained by the 3-D simulation and the two lump models.

The resulting approximate efficiencies are given in Figure 8. Good agreement with the real efficiencies obtained by the CFD simulation can be found.

Double Chamber Case

The net flow rates for the micropump with two chambers operating without phase difference for different back pressures are presented in Figure 9. As in the

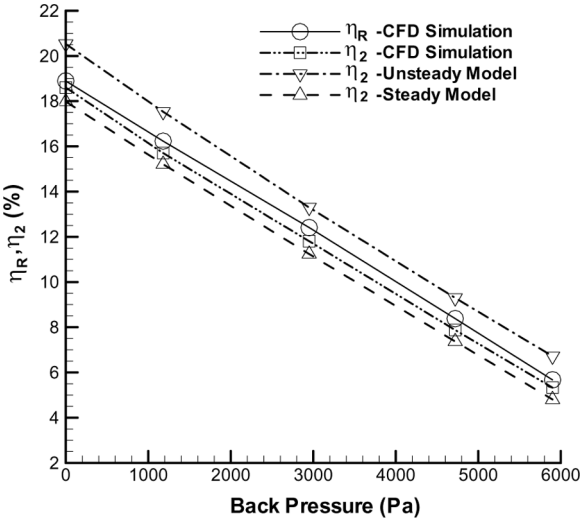

Figure 8. Comparison of predicted efficiencies by the 3-D simulation and the two lump models.

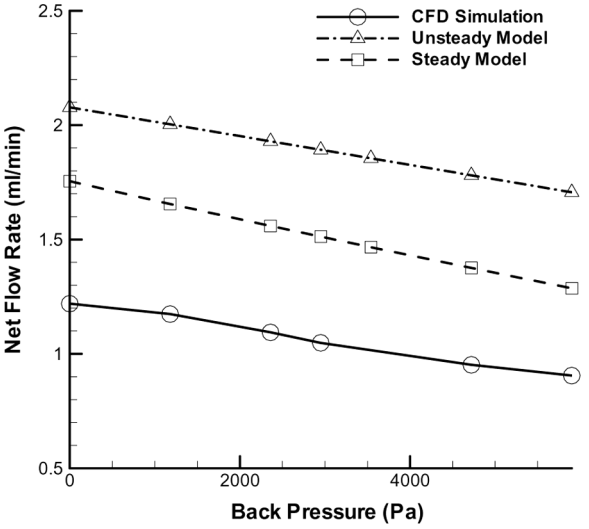

Figure 9. Comparison of predicted net flow rates for the double-chamber case with zero phase angles at various back pressures.

single chamber case, the predicted flow rates by the lump models are higher than the multidimensional calculations. However, the overpredictions are much higher for the double chamber micropump. It is noted that the loss coefficients for the nozzle/diffusers used in the lump models are based on steady-state flows. As will be seen latter, vortices may be formed periodically in the nozzle/diffusers and in the chambers, which will hinder the flow through these elements and, thus, brings about higher loss. This effect is more significant with multiple chambers. Although the net flow rates obtained by the steady model are close to the multidimensional results, it does not mean that the flow characteristics are better depicted by this model. The net pumping rate can be obtained by integrating the instantaneous flow rate through any one of the three nozzle/diffuser elements over one period. As shown in Figure 10, the instantaneous flow rates through the three elements for the unsteady model resemble those obtained by the CFD simulation. This is especially evident by examining the variation of the flow through the center element (Q_c). This flow rate represents the difference between those through the inlet element and the outlet one, i.e., $Q_c = (Q_{\text{in}} + Q_{\text{out}})/2$, which can be yielded by subtracting Eq. (8*b*) from Eq. (8*a*) with $\delta = 0$. The wavy patterns for the unsteady model and the CFD simulation are similar. Both vary in the same phase with a frequency two times that of the member. The values obtained by the two analyses are positive for the entire period, indicating that this center element always plays a function of diffuser for this in-phase operation. The flow rate predicted by the steady model varies in a half-wave form in both the pump stage and the supply stage. Its value is higher than that of the unsteady model in the middle regions of the pump and supply stages, but becomes negative during the transition times between the two stages. This results in lower net flow rate for the steady model than that for the unsteady model after integration and, thus, better agreement with the CFD simulations.

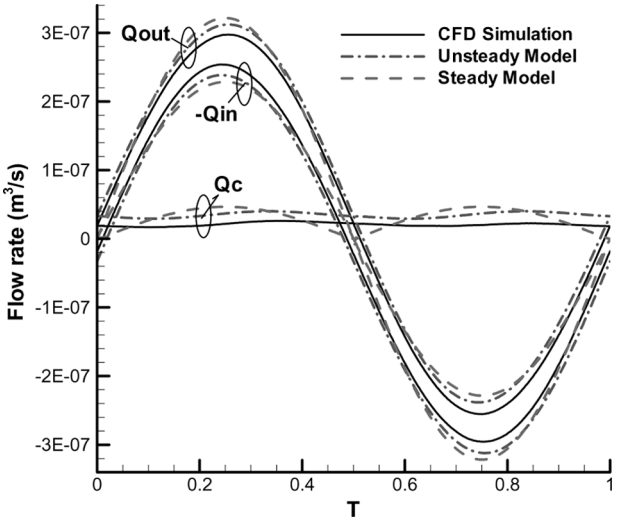

Figure 10. Variation of flow rate for the double-chamber case with zero phase angles.

Comparison of the CFD results shown in Figures 4 and 9 reveals that the net flow rate is slightly increased from 0.99 ml/min for the single chamber pump to 1.22 ml/min for the double chamber pump at zero back pressure. However, the decreasing rate of the latter is much lower when a back pressure is present. At $P_b = 5900$ Pa, the net flow rate is 0.3 ml/min for the single chamber case, comparing with 0.91 ml/min for the double chamber case.

Figure 11 presents the effects of the phase angle between the oscillating membranes of the two chambers for back pressures $P_b = 0$ and 2950 Pa. The net flow rate decreases with the increase of the phase angle until 180°, followed by an increase.

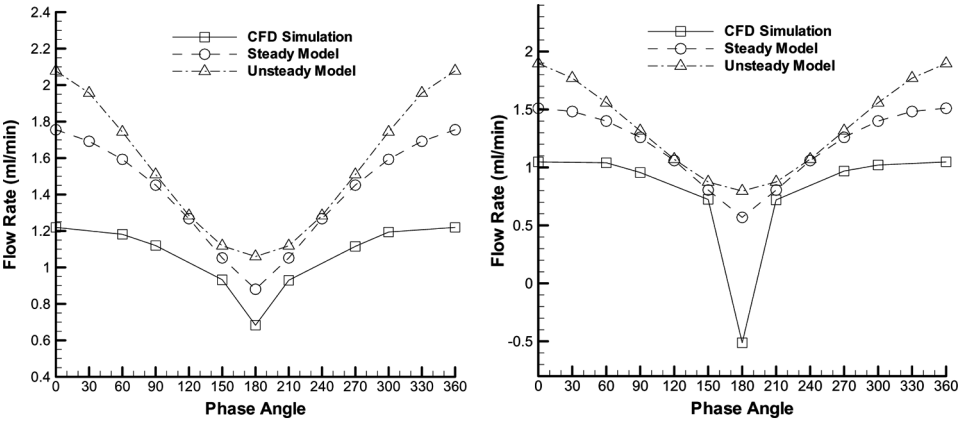

Figure 11. Comparison of predicted net flow rates at various phase angles for (*a*) $P_b = 0$ and (*b*) $P_b = 2950$ Pa.

The variation is symmetrical to the 180°. The results obtained by the different methods behave in a similar fashion, with the simple analyses giving higher net pumping rates. It has been noticed that in the study of Yang et al. [29], the net flow rate for a double chamber micropump varies in a sinusoidal-like manner, with a peak at 90° and negative values for the phase angles greater than 180°. It is believed that the cause of the characteristic difference between the two studies is mainly due to the large difference in compression ratio. The chamber height is 500 μm and the maximum deflection of the membrane is 250 μm in the study of Yang et al., whereas the corresponding values are 200 μm and 1 μm in the present study. The large oscillating amplitude in the study of Yang et al. has considerable effect on the flow in the pump with the resulting flow resistance greatly increased in both the nozzle/diffusers and the chambers. A difference exists in the flow resistance between the two chambers, which varies with the phase angle. However, the resistance is small and the difference can be neglected in the present study because of the small compression ratio.

The variation of the flow rates through the three nozzle/diffusers for phase angles 60° and 150° is given in Figure 12 for $P_b = 2950$ Pa. It can be seen that the amplitudes of Q_{in} and Q_{out} decrease with the increasing phase angle, which leads to a decrease of the net flow. In contrast, the flow rate Q_c gradually increases with the phase angle. The following relation can be derived from Eqs. (8*a*) and (8*b*).

$$Q_c = \frac{1}{2}(Q_{\text{in}} + Q_{\text{out}}) + \frac{V_m \omega}{2}(\sin(\omega t) - \sin(\omega t + \delta)) \tag{20}$$

The second term in the above is negligible for small phase angles. Its importance is increased with the phase angle till 180°. At phase angle of 180°, it becomes a sine function. However, this term does not contribute to the net flow because the integration of it over a period is zero.

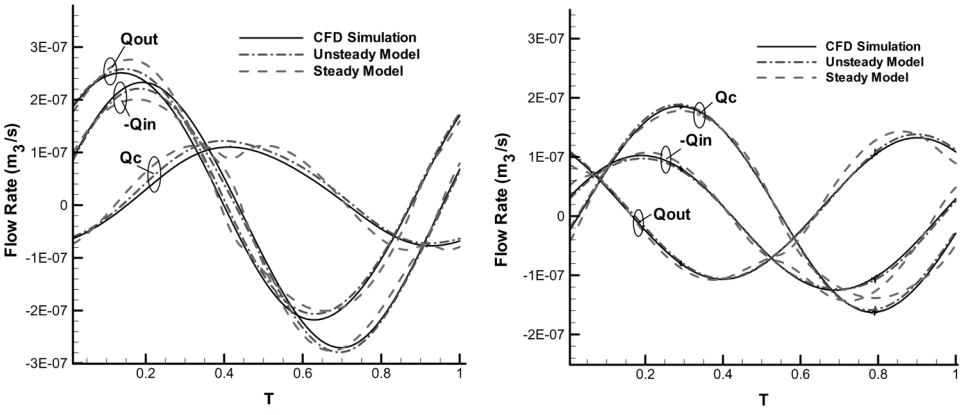

Figure 12. Variation of flow rate at $P_b = 2950$ Pa for the double-chamber case with (*a*) phase angle 60° and (*b*) phase angle 150°.

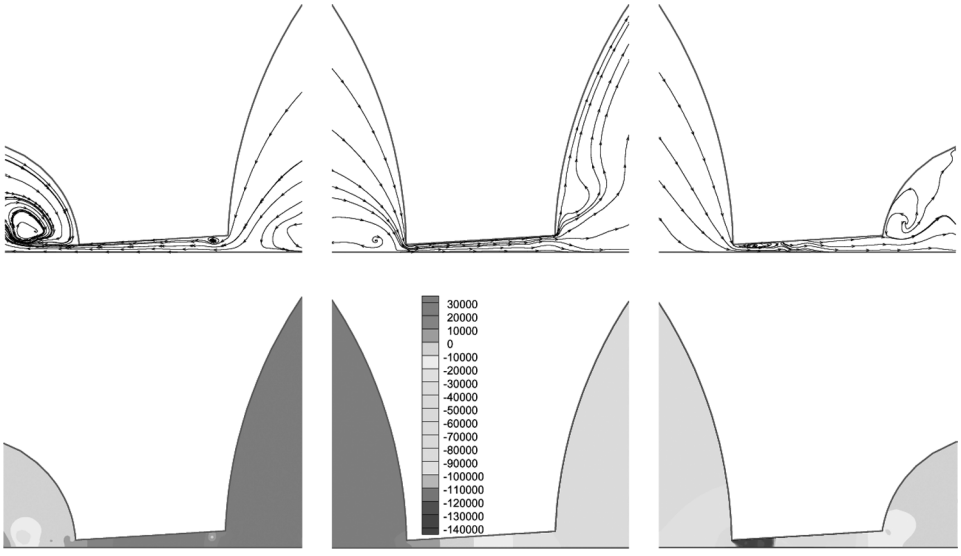

Figure 13. Streamlines and pressure contours at $t = T/4$ for phase angle 60° and $P_b = 0$ Pa.

As an illustration of the flow field, streamlines, and pressure contours at $t = T/4$ and $3T/4$, corresponding to the pump stage and the supply stage, respectively, are shown in Figures 13 and 14 for phase angle 60° and $P_b = 0$. In the pump stage, the flow is directed out of the two main chambers through the inlet part and the outlet part. The inlet channel serves as a nozzle in which the pressure decreases gradually. It can be detected that a small recirculation zone appears at the entrance of the nozzle, where a low pressure region can be identified in the pressure contour plots. The outlet channel functions as a diffuser. Small vortices are located in the

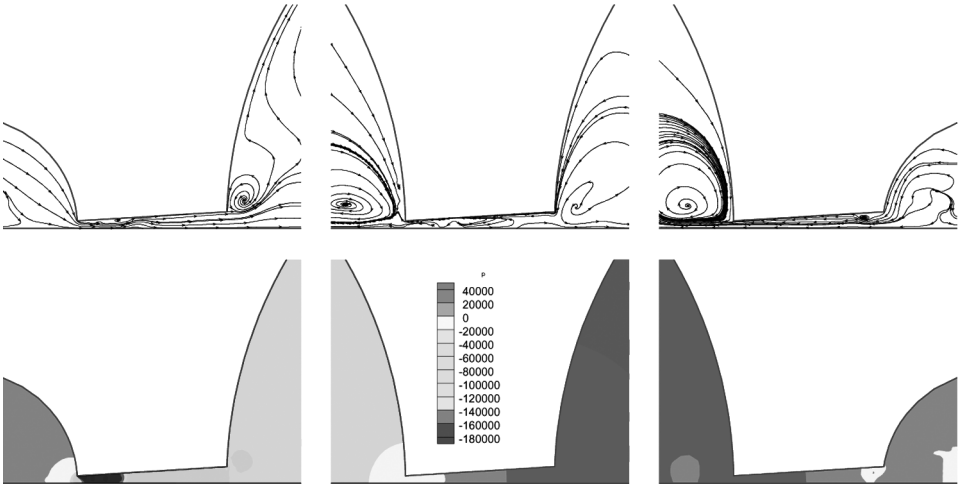

Figure 14. Streamlines and pressure contours at $t = 3T/4$ for phase angle 60° and $P_b = 0$ Pa.

region near the throat. The pressure drops sharply first, followed by gradual recovery. The pressure in the first main chamber is higher than that in the second chamber with the central channel working as a diffuser. There is a large-scale vortex flow in the center region in the first chamber, which forces the flow to make a sharp turn to enter the inlet and the central elements. The recirculating flows in the nozzle/diffusers and the chambers are time-dependent and their appearance will cause additional losses which are not accounted for in the lump models. At the supply stage, the functions of the three elements are reversed. The pressure in the second chamber becomes higher. Small vortices can also be found in the nozzle/diffusers and larger-scale recirculating flows in the chambers.

CONCLUSION

Simple models based on the concept of lumped elements have been developed for analysis of the flow in valveless micropump system. The models overcome the problem of a non-unique solution and allow the use of multiple chambers. The inertial effect was included as an unsteady model. The results show that in comparison with the steady model, the unsteady model can portray the characteristics of the flow in the pumping system more closely as evidenced by comparing with the CFD simulation. The net flows obtained by the lump models are higher than those by the multidimensional calculations due to the complicated recirculating flows in the pump causing additional losses. It was shown that the net pumping flow is increased only marginally when the system is changed from the single chamber to the double chamber. However, the double-chamber system has a higher capability to resist the decline in pumping effectiveness, as back pressures are imposed at the outlet. The net flow is reduced when a phase angle exists between the vibrating membranes of the two chambers. This is in contrast to other studies in which there exists a peak value of net flow at a certain phase angle. The cause of this difference is owing to the insignificant compression ratio assumed in the present pump configuration. For a system with high compression ratio the flow resistance in the pump chamber must be accounted for in the model. Micropumps with three chambers have been seen in biological sample processing and drug delivery applications. The working of these pumping systems is based on the peristalsis concept. Extension of the present models to the peristaltic micropumps is straightforward and such work is under way.

REFERENCES

1. N.-T. Nguyen, X. Huang, and T. K. Chuan, MEMS-Micropumps: A Review, *ASME J. Fluids Eng.*, vol. 24, pp. 384–392, 2002.
2. D. J. Laser and J. G. Santiago, A Review of Micropumps, *J. Micromech. Microeng.*, vol. 4, pp. R35–R64, 2004.
3. P. Woias, Micropumps—Past, Progress and Future Prospects, *Sens. Actuator B*, vol. 105, pp. 28–38, 2005.
4. G. H. Priestman, A Study of Vortex Throttles Part 1: Experimental, *Proc. Inst. Mech. Eng.*, vol. 21, pp. 331–336, 1987a.
5. G. H. Priestman, A Study of Vortex Throttles Part 2: Viscid Flow Analysis, *Proc. Inst. Mech. Eng.*, vol. 21, pp. 337–345, 1987b.

6. A. A. Kulkarni, V. V. Ranade, R. Rajeev, and S. B. Koganti, CFD Simulation of Flow in Vortex Diodes, *AIChE J.*, vol. 54, pp. 1139–1152, 2008.
7. M. Anduze, S. Colin, R. Caen, H. Camon, V. Conedera, and T. Do Conto, Analysis and Testing of a Fluidic Vortex Microdiode, *J. Micromech. Microeng.*, vol. 11, pp. 108–112, 2001.
8. N. Tesla, Vavular Conduit, U.S. Patent No. 1329559, 1920.
9. F. K. Forster, R. L. Bardell, M. A. Afromowitz, N. R. Sharma, and A. Blanchard, Design, Fabrication and Testing of Fixed-Valve Micro-Pumps, In *Proc. of the ASME Fluids Engineering Division*, FED, vol. 234, 1995 IMECE, pp. 39–44, 1995.
10. M. Turowski, Z. Chen, and A. Przekwas, Automated Generation of Compact Models for Fluidic Microsystems, *Analog Integr. Circ. Sig. Process*, vol. 29, pp. 27–36, 2001.
11. A. R. Gamboa, C. J. Morris, and F. K. Forster, Improvements in Fixed-Valve Micropump Performance Through Shape Optimization of Valves, *ASME J. Fluids Eng.*, vol. 127, pp. 339–346, 2005.
12. E. Stemme and G. Stemme, A Valveless Diffuser/Nozzle-Based Fluid Pump, *Sens. Actuator A*, vol. 39, pp. 159–167, 1993.
13. T. Gerlach and H. Wurmus, Working Principle and Performance of the Dynamic Micropump, *Sens. Actuator A*, vol. 50, pp. 135–140, 1995.
14. A. Olsson, G. Stemme, and E. Stemme, Diffuser-Element Design Investigation for Valve-Less Pumps, *Sens. Actuator A*, vol. 57, pp. 137–143, 1996.
15. A. Olsson, G. Stemme, and E. Stemme, Numerical and Experimental Studies of Flat-Walled Diffuser Elements for Valve-less Micropumps, *Sens. Actuator A*, vol. 84, pp. 165–175, 2000.
16. V. Singhal, S. V. Garimella, and J. Y. Murthy, Low Reynolds Number Flow Through Nozzle-Diffuser Elements in Valveless Micropumps, *Sens. Actuator A*, vol. 113, pp. 226–235, 2004.
17. T. Bourouina and J.-P. Grandchamp, Modeling Micopumps with Electrical Equivalent Networks, *J. Micromech. Microeng.*, vol. 6, pp. 398–404, 1996.
18. E. Morganti, I. Fuduli, A. Montefusco, M. Petasecca, and G. U. Pignatel, SPICE Modeling and Design Optimization of Micropumps, *Intern. J. Environ. Anal. Chem.*, vol. 85, pp. 687–698, 2005.
19. A. Ullmann, The Piezoelectric Valve-Less Pump—Performance Enhancement Analysis, *Sens. Actuator A*, vol. 69, pp. 97–105, 1998.
20. A. Olsson, G. Stemme, and E. Stemme, A Numerical Design Study of the Valveless Diffuser Pump using a Lumped-Mass Model, *J. Micromech. Microeng.*, vol. 9, pp. 34–44, 1999.
21. L. S. Pan, T. Y. Ng, G. R. Liu, K. Y. Lam, and T. Y. Jiang, Analytical Solutions for the Dynamic Analysis of a Valveless Micropump—a Fluid-Membrane Coupling Study, *Sens. Actuator A*, vol. 93, pp. 173–181, 2001.
22. L. S. Pan, T. Y. Ng, X. H. Wu, and H. P. Lee, Analysis of Valveless Micropumps with Inertial Effects, *J. Micromech. Microeng.*, vol. 13, pp. 390–399, 2003.
23. A. Ullmann, I. Fono, and Y. Taitel, A Piezoelectric Valve-Less Pump—Dynamic Model, *ASME J. Fluids Eng.*, vol. 123, pp. 92–98, 2001.
24. A. Ullmann and I. Fono, The Piezoelectric Valve-Less Pump—Improved Dynamic Model, *J. Microelectromech. Syst.*, vol. 11, pp. 655–664, 2002.
25. Y.-Y. Tsui and S.-L. Lu, Evaluation of the Performance of a Valveless Micropump by CFD and Lumped-System Analyses, *Sens. Actuator A*, vol. 148, pp. 138–148, 2008.
26. Y.-Y. Tsui and Y.-F. Pan, A Pressure-Correction Method for Incompressible Flows using Unstructured Meshes, *Numer. Heat Transfer B*, vol. 49, pp. 43–65, 2006.

27. Y.-Y. Tsui and T.-C. Wu, A Pressure-Based Unstructured-Grid Algorithm using High-Resolution Schemes for All-Speed Flows, *Numer. Heat Transfer B*, vol. 53, pp. 75–96, 2008.
28. R. I. Issa, Solution of the Implicitly Discretised Fluid Flow Equation by Operator-Splitting, *J. Comput. Physics*, vol. 62, pp. 40–65, 1986.
29. K.-S. Yang, I.-Y. Chen, and C.-C. Wang, Performance of Nozzle/Diffuser Micro- Pumps Subject to Parallel and Series Combinations, *Chem. Eng. Technol.*, vol. 29, pp. 703–710, 2006.